RESEARCH ON THE CHARACTERISTICS OF DISPERSION AND ATTENUATION IN HYDRATE-BEARING FORMATIONS BASED ON BIOT'S THEORY

PENGQI LIU[1,2,3], HANDONG HUANG[3], SHUANG MAO[4,5], LIGUO HU[5],
CHAO WANG[6] and SUO CHENG[6]

[1] *Sanya Institute of South China Sea Geology, Guangzhou Marine Geological Survey, Sanya, P.R. China. 376097096@qq.com*
[2] *Academy of South China Sea Geological Science, China Geological Survey, Sanya, P.R. China.*
[3] *State Key Laboratory of Petroleum Resources and Prospecting, China University of Petroleum-Beijing, Beijing, P.R. China.*
[4] *Yangtze University, Wuhan, P.R. China.*
[5] *PetroChina Liaohe Oilfield Company, Panjin, P.R. China.*
[6] *Research Institute of Exploration and Development, Tarim Oilfield Company, PetroChina, Korla, P.R. China.*

(Received January 7, 2022; revised version accepted Augsut 1, 2022)

ABSTRACT

Liu, P.Q., Huang, H.D., Mao, S., Hu, L., Wang, C. and Cheng, S., 2022. Research on the characteristics of dispersion and attenuation in hydrate-bearing formations based on Biot's theory. *Journal of Seismic Exploration*, 31: 451-477.

Previous studies have shown that P-wave velocity and S-wave velocities increase as increasing hydrate saturation. However, the characteristics of dispersion and attenuation of hydrate-bearing formation are still controversial. Based on Biot's theory, this paper clarifies the characteristics of hydrate formation's dispersion and attenuation in suspension, particle-support, and cementation modes. The results show that hydrate's occurrence mode and saturation affect the dispersion and attenuation. For the P-wave, the peak value of attenuation and frequency curve increases with the increasing saturation in suspension and particle-supported modes. The peak value increases with increasing hydrate saturation when the hydrate saturation is less than 0.28 and decreases with increasing hydrate saturation when the hydrate saturation is larger than 0.28. For the S-wave, the peak value decreases with increasing hydrate saturation in suspension, particle-support, and cementation modes.

KEY WORDS: gas hydrate, saturation, Biot's theory, dispersion, attenuation.

0963-0651/22/$5.00

NOMENCLATURE LIST

pressure wave (P-wave)
shear wave (S-wave)
natural gas hydrate (NGH)
offshore drilling platform (ODP)
quality factor (Q)
vertical seismic profile (VSP)
Biot and squirt flow (BISQ)
Hertz (Hz)
Natural Science Foundation of China (NSFC)

INTRODUCTION

Natural gas hydrate (NGH), also known as "combustible ice," is an ice-like crystalline substance formed by natural gas and water under high pressure and low temperature in deep-sea sediments or land permafrost. It has attracted much attention because of its tremendous energy, climate, environment, and geohazard value. The effect of hydrate on velocity has been well understood. Researchers at home and abroad have put forward many theories or experimental models to estimate hydrate saturation by linking hydrate saturation and velocity. There are two main categories considered in the method. The first is the empirical formula method. They are time - average equation (Wyllie et al., 1956), wood equation (Wood et al., 1994), and weighted equation (Lee et al., 1996). The second kind is namely the effective medium method (Helgerud, 1999; Dvorkin, 1996). The common conclusion is that the P-wave and S-wave velocities increase in different trends with hydrate saturation.

The research on the attenuation and dispersion of hydrate reservoirs is still controversial. Some researchers believe that the attenuation decreases with the increasing hydrate saturation. Wood et al. (2000) noted that the increased attenuation observed in the ODP 164 vertical seismic profile was due to the freezing of fine mud and suggested that hydrates may have reduced the attenuation. Rossi et al. (2007) used the tomographic inversion algorithm based on the frequency-shift method to estimate the quality factor Q from the seismic reflection waves. It is considered that hydrate can cement the grains, and the attenuation decreases with the increase of hydrate saturation. Sain et al. (2009) pointed out that hydrate, as a particle cement of sediments, would increase the strength of sediments and thus reduce the seismic wave attenuation. Jaiswal et al. (2012) estimated the quality factor Q based on the full waveform inversion algorithm. Research shows that the presence of hydrates reduces the seismic attenuation of fine-grained sediments. Dewangan et al. (2014) analyzed some samples containing natural hydrates and indicated that the presence of hydrates reduced attenuation.

Some researchers believe that the attenuation increases with increasing hydrate saturation. Sakai (1999) pointed out that the Mallik well in northern Canada is in the gas hydrate section, where the VSP shear signal may be strongly weakened. Using acoustic logs from the Mallik tundra, Guerin and

Goldberg (2002) calculated P-wave and S-wave attenuation using the centroid frequency migration method. It is found that both of them present high attenuation values in hydrate-bearing formations. It is considered that the attenuation of the amplitude of acoustic waves in the hydrate formation is caused by the strong absorption characteristics of the formation. They conducted an intersection analysis of hydrate saturation and P-wave attenuation. They concluded that P-wave attenuation is roughly linear with hydrate saturation, and S-wave attenuation is larger than P-wave attenuation under the same hydrate saturation condition. Using the cross-well seismic data, Pratt et al. (2005) used the tomographic technique to image the attenuation profile of the cross-well seismic data between two Wells. The results show that the attenuation of seismic waves in hydrate formation also indicates a significant anomaly of high value. The attenuation curves calculated by Guerin and Goldberg (2002) are the absorption properties at very high frequencies (1-20 kHz). At the same time, Pratt et al. (2005) analyzed the absorption properties of seismic waves at a relatively low-frequency range (200-2000 Hz). This is an essential complement to the results of the analysis by Guerin and Goldberg (2002). Pecher et al. (2003) suggest that hydrate acts as a cement to increase velocity and attenuation. According to Dvorkin (2004), an increase in hydrate concentration will increase the elastic heterogeneity of the formation, which will cause the cross-flow of pore fluid between the hard and soft domains of the rock resulting in seismic wave attenuation. Gerner et al. (2007) studied attenuation using the pore elasticity model. It is considered that when the pore space is partially saturated with hydrate, the attenuation increases due to the limited fluid flow. Zhang (2016) studied the nonlinear variation trend of P-wave and S-wave of unconsolidated marine hydrate-bearing sediments based on the effective medium theoretical model. The results show that the velocity and attenuation increase with the increasing hydrate saturation.

In addition, some researchers have other views. Matsushima (2006) noted that there was no significant increase in the attenuation of the hydrate layer by examining VSP data in the South Sea Trough of Japan. Priest et al. (2006) measured the attenuation values of 13 sandstone specimens containing hydrates of different saturation by synthesizing them in the laboratory. The results show that when the hydrate saturation is less than 3%~5%, the P-wave attenuation rapidly increases to the maximum value with the increase of saturation, decreases quickly, and then presents a slow increase trend. According to Priest et al. (2006), the hydrate sandstone samples synthesized in the laboratory are partially saturated rock, consisting of four phases: rock skeleton, hydrate, adsorbed water, and free gas. Before hydrate formation, the propagation of seismic waves causes water and free gas in rock fractures and pores to undergo adsorption mechanisms and thus generate jet streams, resulting in the attenuation of seismic wave energy. When hydrates are formed, they bond to the rock skeleton and increase the length of fractures and pores, resulting in more intense attenuation. This effect reaches its maximum when the hydrate saturation reaches the critical saturation. With the further increase of hydrate saturation, the cement between hydrate and rock will gradually completely plug the cracks and voids, and the adsorbed water and free gas will be bound, and the squirting flow effect will be weakened, so the absorption will gradually weaken. Lee and Waite (2007) pointed out that the attenuation of acoustic signals in the Mallik area may be caused by the coupling of seismic sources rather than hydrate. Li (2015) studied the attenuation characteristics of seismic waves in hydrate-bearing formation at micro and mesoscale based on BISQ and White seismic wave attenuation models in porous media, respectively. The results show that seismic wave attenuation increases with the increase of hydrate formation in the ultrasonic frequency band but decreases with the increase of hydrate saturation in the seismic exploration frequency band. This conclusion is consistent with Sain (2009). Sun et al. (2014) compared the P-wave attenuation models. They pointed out that the wave-induced oscillatory fluid flow near the inclusion in porous rock was one of the main reasons for the dispersion and attenuation of P-wave at seismic frequency. Sahoo et al. (2018) and Marin-Moreno (2017) believe that under the stable condition of NGH, natural gas and hydrate coexist, and the presence of gas itself will have a strong impact on attenuation. Through experiments, Sourav et al. (2019) showed that when hydrate saturation is lower than 6%, attenuation increases with measurement frequency. The attenuation decreases with frequency when the hydrate saturation is higher than 6%. Through rock physics simulation, Guo (2021) pointed out that the P-wave velocity is not sensitive to the increase of hydrate saturation under the pore filling mode. However, P-wave velocity increases rapidly with the increasing hydrate saturation in the coexistence mode of pore filling and particle cementation.

Previous studies have studied the dispersion and attenuation of hydrate formation through observation data, simulation experiments, and theoretical derivation. The conclusions are different. Some reseachers believe that hydrates increase formation attenuation, some believe that hydrates decrease formation attenuation, and some have obtained other understandings. No research has been conducted on the dispersion and attenuation of hydrate formations with different occurrence modes. Based on Biot's theory, this paper studies the relationship between hydrate saturation and dispersion and attenuation under suspension mode, particle-supported mode, and cement mode for the first time and clarifies each mode's dispersion and attenuation rules. This study can provide a reference for the quantitative characterization of hydrates.

METHOD

Hydrate occurrence model and Biot's theory

There may be contact or no contact between hydrate and particles, and there are numerous microscopic occurrence modes in hydrate formation. This paper focuses on three modes, which are suspension mode, particle-supported mode, and cementation mode corresponding to A, B, and C, respectively (see Fig. 1) (Ecker, 2001). These different modes affect the petrophysical characteristics of hydrate deposits. In mode A, the hydrate is suspended in the pores and only impacts the bulk modulus of the sediment.

The presence of hydrates in the fluid-saturated pore space increases the effective bulk modulus of the mixture and consequently the bulk modulus of the saturated rock. According to Gassmann's theory, the shear modulus is not affected. In mode B, the hydrate is a part of the rock skeleton, which reduces the porosity. The reduction in porosity increases the stiffness of the skeleton and increases the bulk modulus to a certain extent. Mode C is similar to mode B. However, the bulk modulus and stiffness increase is much larger than in mode B.

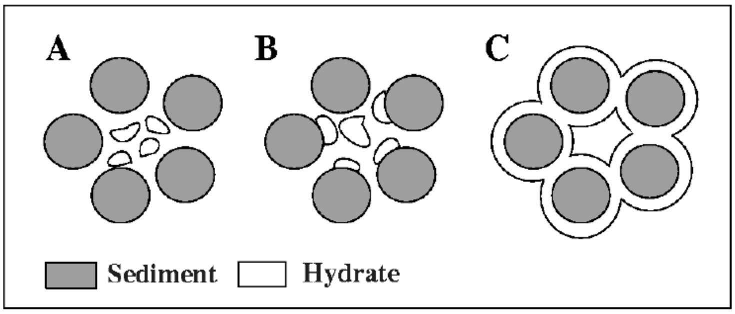

Fig. 1. Three microscopic occurrence patterns of natural gas hydrates. Mode A represents hydrate being a part of the fluid. In mode B, hydrate is part of the solid frame. Mode C assumes that hydrate cements the grains evenly sat-hydrate. (Ecker, 2001).

The effective medium theory and Biot-Gassmann formulation show the relationship between P-wave velocity and saturation theory in three microscopic occurrence modes (Fig. 2). It can be observed that the P-wave velocity increases with the increasing hydrate saturation under the three occurrence modes. At the same saturation, the P-wave impedance of modes A, B, and C increases in turn. For mode C, a small amount of hydrate can significantly increase the P-wave velocity of the medium, while the growth rate of mode B and mode A is relatively slow.

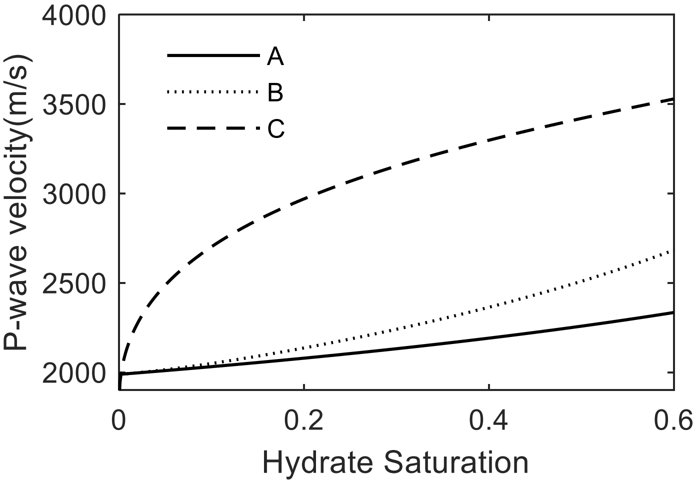

Fig. 2. Hydrate saturation versus P-wave velocity for three microscopic modes. A is the suspension mode, B is the particle-supported mode, and C is the cementation mode.

Biot (1956) deduced the theoretical formulas of frequency-dependent velocities in fluid-saturated porous rock. The theoretical formulae include the mechanisms of viscous and inertial interactions between pore fluids and mineral skeletons. The theory contains the following assumptions. A) The wavelength is much larger than that of the studied macroscopic volume element, and the pore size is much smaller than that of the macroscopic volume element. B) The displacement of both the fluid and solid phases is small. That is, the deformation generated by the medium is slight. C) The fluid phase in the pore space is in constant porosity, full saturation, and macroscopic isotropy. D) In generalization to the anisotropic elastic case, the matrix is assumed to be isotropic, and the mechanism of matrix-related viscosity is not discussed. E) The pore fluid is assumed to conform to Darcy's flow law.

The entire frequency relationship of Biot's theory is as follows (Biot, 1956):

$$\begin{vmatrix} H/V_p^2-\rho & \rho_f-C/V_p^2 \\ C/V_p^2-\rho_f & q-M/V_p^2 \end{vmatrix}=0\,; \quad \begin{vmatrix} \rho-G_{fr}/V_s^2 & \rho_f \\ \rho_f & q \end{vmatrix}=0\ . \tag{1}$$

Complex root is as follows:

$$\frac{1}{V_p^2}=\frac{-\left(Hq+M\rho-2C\rho_f\right)\pm\sqrt{\left(Hq+M\rho-2C\rho_f\right)^2-4\left(C^2-MH\right)\left(\rho^2-\rho q\right)}}{2\left(C^2-MH\right)}\ , \tag{2}$$

$$\frac{1}{V_S^2}=\frac{\rho q-\rho_f}{qG_{fr}}\ , \tag{3}$$

where V_P is the P-wave velocity, in m/s; V_S is the S-wave velocity, in m/s; ρ is the formation volume density, in Kg/m^3; ρ_f is the fluid density, in Kg/m^3; G_{fr} is the Shear modulus of rock, in Pa. The real and imaginary parts of the root represent the corresponding velocity and attenuation, respectively. In the two solutions of P-wave, the sign + corresponds to fast P-wave, and the sign - corresponds to slow P-wave. V_P and V_S are complex velocities. The expressions for the other items are as follows:

$$H=K_{fr}+\frac{4}{3}G_{fr}+\frac{\left(K_0-K_{fr}\right)^2}{D-K_{fr}}\ , \tag{4}$$

$$C=\frac{\left(K_0-K_{fr}\right)K_0}{D-K_{fr}}\ , \tag{5}$$

$$M = \frac{{K_0}^2}{D - K_{fr}} \ , \tag{6}$$

$$D = K_0 \left[1 + \phi \left(K_0 / K_{fr} - 1 \right) \right] \ , \tag{7}$$

$$\rho = \left(1 - \phi\right) \rho_0 + \phi \rho_f \ , \tag{8}$$

$$q = \frac{\alpha \rho_f}{\phi} - \frac{i \eta F\left(\zeta\right)}{\omega \kappa} \ , \tag{9}$$

$$F\left(\zeta\right) = \frac{1}{4} \frac{\zeta T\left(\zeta\right)}{1 + i T\left(\zeta\right) / \zeta} \ , \tag{10}$$

$$T\left(\zeta\right) = \frac{ber'\left(\zeta\right) + iber'\left(\zeta\right)}{ber\left(\zeta\right) + iber\left(\zeta\right)} = \frac{e^{i3\pi/4} J_1\left(\zeta e^{-i\pi/4}\right)}{J_0\left(\zeta e^{-i\pi/4}\right)} \ , \tag{11}$$

$$\zeta = \left(\frac{\omega a^2 \rho_f}{\eta} \right)^{0.5} \ , \tag{12}$$

where K_{fr} is the bulk modulus of dry rock, Pa; K_0 is the bulk modulus of mineral, ρ_0 is the density of mineral, Pa; ϕ is porosity; α is sinuosity, dimensionless; η is Pore fluid viscosity, $\mathrm{Pa} \cdot \mathrm{s}$; κ is absolute rock permeability, m^2; f is frequency, Hz; $F\left(\zeta\right)$ is viscous dynamic operator; ω is angular frequency of plane wave, $\omega = 2\pi f$; $ber(\ )$ and $ber'(\ )$ are the real and imaginary parts of Kelvin function, respectively; J_n is Bessel functions of order n; a is aperture parameters, m.

The tortuosity α (sometimes called the structure factor) is a purely geometric factor independent of solids or fluids (Berryman, 1981):

$$\alpha = 1 - r(1 - 1/\phi) \ . \tag{13}$$

For sphere, r = 0.5, and for ellipsoids is between 0 and 1. For cylindrical pores whose axes are parallel to the pore pressure gradient, a = 1 (minimum possible value). For a random system with all possible distribution of pores, $\alpha = 3$ (Stoll, 1977). The high frequency limit velocity depends on the size of a, and there is a negative correlation between the two. In this study, r is 0.5.

Aperture parameters are related to pore size and shape. Hovem and

Ingram (1979) used the following formula to calculate the aperture parameters:

$$a = \phi d / \left[3\left(1-\phi\right)\right] \ , \tag{14}$$

where *d* stands for particle diameter, m.

Biot's critical frequency is defined as follows:

$$f_c = \frac{\phi \eta_f}{2\pi \rho_f \kappa} \ , \tag{15}$$

The Biot's critical frequency is defined as the frequency when the viscous force applied to the pore fluid is approximately equal to the inertial force. It determines the low frequency range ($f = f_c$) and high frequency range (f ? f_c). In the high frequency range, the fluid is mainly controlled by inertia action, and in the low frequency range, the fluid is mainly controlled by viscosity action.

The absolute permeability of rock is formulated as follows (Hovem and Ingram, 1979):

$$\kappa = (d^3 / 36k)\left[\phi^3 / \left(1-\phi\right)^2\right] \ , \tag{16}$$

where k is the physical quantity related to pore shape and pore curvature degree. For spherical particles, both theory and experiment confirm $k \approx 5$.

The low frequency limit velocities of fast P-wave and fast S-wave are calculated by Gassmann equation:

$$V_{PLFL} = \sqrt{\frac{(\mathrm{K}_{sat} + 4\,\mathrm{G}_{sat})}{\rho}} \ , \tag{17}$$

$$V_{SLFL} = \sqrt{\frac{\mathrm{G}_{sat}}{\rho}} \ , \tag{18}$$

$$\rho = (1-\phi)\rho_0 + \phi\rho_f \ , \tag{19}$$

$$K_{sat} = K_0 \frac{\phi K_{Dry} - (1+\phi)\mathrm{K}_f K_{Dry} / \mathrm{K}_0 + \mathrm{K}_f}{(1-\phi)\mathrm{K}_f + \phi K_0 - \mathrm{K}_f \mathrm{K}_{Dry} / K_0} \ , \tag{20}$$

$$G_{sat} = G_{Dry} \ , \tag{21}$$

where K_{sat} and G_{sat} are the bulk modulus and shear modulus of saturated rock, respectively, Pa. K_f is the bulk modulus of formation fluid, Pa; K_0 is the bulk modulus of the skeleton particles, Pa.

The high frequency limit velocities of P-wave and S-wave are formulated by Johnson and Plona (1982):

$$V_{PHFL}\left(fast,slow\right)=\left\{\frac{\Delta\pm\left[\Delta^2-4\left(\rho_{11}\rho_{22}-\rho_{12}^2\right)\left(PR-Q^2\right)\right]^{0.5}}{2\left(\rho_{11}\rho_{22}-\rho_{12}^2\right)}\right\}^{0.5}, \tag{22}$$

$$V_{SHFL}=\left(\frac{G_{fr}}{\rho-\phi\rho_f\alpha^{-1}}\right)^{0.5}, \tag{23}$$

$$\Delta=P\rho_{22}+R\rho_{11}-2Q\rho_{12}\ , \tag{24}$$

$$P=\frac{\left(1-\phi\right)\left(1-\phi-K_{fr}/K_0\right)K_0+\phi K_0K_{fr}/K_f}{1-\phi-K_{fr}/K_0+\phi K_0/K_f}+\frac{4}{3}G_{fr}\ , \tag{25}$$

$$Q=\frac{\left(1-\phi-K_{fr}/K_0\right)\phi K_0}{1-\phi-K_{fr}/K_0+\phi K_0/K_f}\ , \tag{26}$$

$$R=\frac{\phi^2K_0}{1-\phi-K_{fr}/K_0+\phi K_0/K_f}\ , \tag{27}$$

$$\rho_{11}=\left(1-\phi\right)\rho_0-\left(1-\alpha\right)\phi\rho_f\ , \tag{28}$$

$$\rho_{22}=\alpha\phi\rho_f\ , \tag{29}$$

$$\rho_{12}=\phi\rho_f-\alpha\phi\rho_f\ , \tag{30}$$

$$\rho=\rho_0\left(1-\phi\right)+\rho_f\phi\ . \tag{31}$$

where ρ_{12} represents the induced mass generated by the relative acceleration of inertial traction between the solid skeleton and the pore fluid, in Kg/m^3.

Mode A

Based on the Hertz-Mindlin theory (Mindlin, 1949), Dvorkin (1996) proposed a velocity model for uncemented, high-porosity hydrate-bearing deposition media and gave the expression of bulk modulus and shear modulus of dry rock.

, $$K_{Dry} = \begin{cases} \left(\dfrac{\phi/\phi_0}{K_{HM} + \frac{4}{3}G_{HM}} + \dfrac{1-\phi/\phi_0}{K_0 + \frac{4}{3}G_{HM}} \right)^{-1} - \dfrac{4}{3}G_{HM}, \phi < \phi_0 \\ \left[\dfrac{(1-\phi)/(1-\phi_0)}{K_{HM} + \frac{4}{3}G_{HM}} + \dfrac{(\phi-\phi_0)/(1-\phi_0)}{\frac{4}{3}G_{HM}} \right]^{-1} - \dfrac{4}{3}G_{HM}, \phi \geq \phi_0 \end{cases} \quad (32)$$

$$G_{Dry} = \begin{cases} \left(\dfrac{\phi/\phi_0}{G_{HM} + Z} + \dfrac{1-\phi/\phi_0}{G_0 + Z} \right)^{-1} - Z, \phi < \phi_0 \\ \left[\dfrac{(1-\phi)/(1-\phi_0)}{G_{HM} + Z} + \dfrac{(\phi-\phi_0)/(1-\phi_0)}{Z} \right]^{-1} - Z, \phi \geq \phi_0 \end{cases}, \quad (33)$$

$$Z = \frac{G_{HM}}{6}\left(\frac{9K_{HM} + 8G_{HM}}{K_{HM} + 2G_{HM}} \right), \quad (34)$$

$$K_{HM} = \left[\frac{n^2(1-\phi_0)^2 G_0^2}{18\pi^2(1-\nu_0)^2} P \right]^{\frac{1}{3}}; \quad G_{HM} = \frac{5-4\nu_0}{5(2-\nu_0)} \left[\frac{3n^2(1-\phi_0)^2 G_0^2}{2\pi^2(1-\nu_0)^2} P \right]^{\frac{1}{3}}, \quad (35)$$

where ϕ_0 is the critical porosity (ϕ_0= 0.36-0.40) (Nur et al., 1998). K_{HM} and G_{HM} represent the effective bulk modulus and shear modulus of dry rock when rock porosity is critical, respectively. G_0 and v_0 represent the shear modulus and Poisson's ratio of skeleton particles, respectively. n is the average number of particles in contact per unit volume (generally 8 or 9) (Dvorkin and Nur, 1996). P is the effective pressure, which is generally calculated according to the following formula:

$$P = (1-\phi)(\rho_0 - \rho_f)gh, \quad (36)$$

where g is gravitational acceleration, m/s^2. h is depth below seafloor, m.

When $\phi = \varphi_0$, the bulk modulus K_{Dry} and shear modulus of dry rock G_{Dry} are calculated by formula (35). When $\phi \neq \phi_0$, K_{Dry} and G_{Dry} are calculated using formulas (32)-(33).

Fluid bulk modulus K_f:

$$K_f = \left[\frac{(1-S_h)}{K_w} + \frac{S_h}{K_h} \right]^{-1}, \quad (37)$$

K_w and K_h represent the bulk modulus of formation water and hydrate, respectively, Pa; S_h is hydrate saturation.

The formation fluid density ρ_f :

$$\rho_f = (1 - S_h)\rho_w + S_h\rho_h \quad , \tag{38}$$

ρ_w and ρ_h represent formation water density and hydrate density, respectively, Kg/m^3.

Formation density ρ :

$$\rho = (1-\phi)\rho_0 + \phi\rho_f \quad , \tag{39}$$

The fluid viscosity η_f was concluded by Balakin through experimental data fitting (Balakin, 2010):

$$\eta_f = \eta_w \left(1 - S_h\right)^{-2.55} \quad . \tag{40}$$

where η_w is the viscosity of formation water, Pa · s. The aperture parameters, permeability and tortuosity are calculated by using eqs. (13), (14) and (16).

Mode B

Compared with mode A, hydrate is considered part of the rock skeleton in the particle-supported model. This has two effects. One is to change the bulk and shear modulus of the skeleton, and the other is to reduce the formation's porosity.

The equivalent bulk modulus and shear modulus of skeleton particles are as follows:

$$K_s = f_h K_h + \left(1 - f_h\right) K_0 , \tag{41}$$

$$G_s = f_h G_h + \left(1 - f_h\right) G_0 \quad , \tag{42}$$

where, f_h is the percentage of hydrate in the solid phase：

$$f_h = \phi S_h / \left[1 - \phi\left(1 - S_h\right)\right] \quad , \tag{43}$$

The equivalent skeleton particle density is as follows:

$$\rho_s = \frac{\left(1-\phi\right)\rho_0 + \phi S_h \rho_h}{1 - \phi + \phi S_h} \quad . \tag{44}$$

The formation porosity is as follows：

$$\phi = \phi_v\left(1 - S_h\right) \quad , \tag{45}$$

where ϕ_v is the porosity of virgin zone, that is, the formation without hydrate.

The formation effective pressure is as follows:

$$P = \left(1 - \phi\right)\left(\rho_s - \rho_w\right)gh \quad , \tag{46}$$

The bulk modulus and shear modulus of formation pore fluid are as follows：

$$K_f = K_w ; \; G_f = 0 \quad . \tag{46}$$

Mode C

For the cemented model, the formation's porosity decreases after the formation contain hydrate, and the bulk modulus and shear modulus of the dry rock skeleton both change.

$$\phi = \phi_v\left(1 - S_h\right) \quad , \tag{47}$$

According to the theory of cementation (Dvorkin and Nur, 1996):

$$K_{Dry} = \frac{1}{6} n\left(1 - \phi_{\mathrm{v}}\right)\left(K_h + \frac{4}{3} G_h\right) S_n \quad , \tag{48}$$

$$G_{Dry} = \frac{3}{5} K_{Dry} + \frac{3}{20} n\left(1 - \phi_{\mathrm{v}}\right) G_h S_\tau \quad , \tag{49}$$

where S_n and S_τ are directly proportional to the normal and shear stiffness of the cemented two particle assemblies, respectively, which depends on the content of the cemented material. The properties of cements and particles are determined by the following relationship:

$$S_n = A_n {r_{cp}}^2 + B_n r_{cp} + C_n \quad , \tag{50}$$

$$A_n = -0.024153 \Lambda_n^{-1.3646} \quad , \tag{51}$$

$$B_n = 0.20405 \Lambda_n^{-0.89008} \quad , \tag{52}$$

$$C_n = 0.00024649 \Lambda_n^{-1.9864} \quad , \tag{53}$$

$$S_\tau = A_\tau {r_{cp}}^2 + B_\tau r_{cp} + C_\tau \quad , \tag{54}$$

$$A_\tau = -10^{-2}\left(2.26\nu^2 + 2.07\nu + 2.3\right)\Lambda_\tau^{0.079\nu^2+0.1754\nu-1.342} \quad , \tag{55}$$

$$B_\tau = \left(0.0573\nu^2 + 0.0937\nu + 0.202\right)\Lambda_\tau^{0.0274\nu^2+0.0529\nu-0.8765} \quad , \tag{56}$$

$$C_\tau = 10^{-4}\left(9.654\nu^2 + 4.945\nu + 3.1\right)\Lambda_\tau^{0.01867\nu^2+0.4011\nu-1.8186} \quad , \tag{57}$$

$$\Lambda_n = \frac{2G_h}{\pi G_0}\frac{\left(1-\nu_0\right)\left(1-\nu_h\right)}{1-2\upsilon_h}, \quad \Lambda_\tau = \frac{G_h}{\pi G_0}, \quad r_{cp} = \left[\frac{2S_h\phi_v}{3\left(1-\phi_v\right)}\right]^{0.5} \quad , \tag{58}$$

where G_0 and ν_0 are Shear modulus and Poisson's ratio of skeleton particles, ν_h is the Poisson ratio of the cement (hydrate), r_{cp} is the ratio of the radius of the cement layer to the radius of the particle.

When the formation is filled with hydrate, Hill's average formula (Hill, 1952) is used to obtain the equivalent bulk modulus and shear modulus of skeleton particles

$$K_s = \frac{1}{2}\left\{f_h K_h + \left(1-f_h\right)K_0 + \left[f_h / K_h + \left(1-f_h\right)K_0\right]^{-1}\right\} \ , \tag{59}$$

$$G_s = \frac{1}{2}\left\{f_h G_h + \left(1-f_h\right)G_0 + \left[f_h / G_h + \left(1-f_h\right)G_0\right]^{-1}\right\} \ , \tag{60}$$

The percentage of hydrate in the solid phase：

$$f_h = \phi_v S_h / \left[1-\phi_v\left(1-S_h\right)\right]) \ , \tag{61}$$

The equivalent skeleton particle density is as follows:

$$\rho_s = \frac{\left(1-\phi_v\right)\rho_0 + \phi_v S_h \rho_h}{1-\phi_v + \phi_v S_h} \quad , \tag{62}$$

The existing porosity of the formation is as follows：

$$\phi = \phi_v\left(1-S_h\right) \ , \tag{63}$$

The bulk modulus and shear modulus of formation pore fluid are as follows:

$$K_f = K_w ; \quad G_f = 0 \ . \tag{64}$$

RESULTS AND DISCUSSIONS

The dispersion and attenuation are calculated separately for mode A, B and C using the above equations.

Mode A

Fig. 3 shows the variation characteristics of P-wave velocity with frequency. For different hydrate saturation, the P-wave velocity increases non-linearly with the increasing frequency, and the P-wave velocity increases overall with the increasing hydrate saturation. The P-wave velocities in the low-frequency range and high-frequency range are almost unchanged. The P-wave velocity near the characteristic frequency increases rapidly to a specific value, and the amount of dispersion is positively correlated with hydrate saturation. Fig. 4 and Fig. 7 show the variation characteristics of the P-wave attenuation coefficient, which is the inverse of the quality factor with frequency. The attenuation increase first and then decreases with the increasing hydrate saturation and reaches the peak at the characteristic frequency. With the increase of saturation, the peak value of the curve of attenuation and frequency gradually increases and moves to the right. Fig. 5 shows the variation characteristics of S-wave velocity with frequency. For different hydrate saturation, the S-wave velocities increase non-linearly with the increasing frequency, and the S-wave velocities generally increase with the increasing saturation. S-wave velocities in the low-frequency range and high-frequency range are almost unchanged. The P-wave velocity increases rapidly to a specific value near the characteristic frequency, and the increasing amplitude is negatively correlated with hydrate saturation. Fig. 6 and Fig. 8 reflect the variation characteristics of the S-wave attenuation coefficient with frequency. The attenuation increase first and then decreases with the increasing hydrate saturation and reaches the peak near the characteristic frequency. With the saturation increase, the peak value of the attenuation and frequency curve gradually decreases and moves to the right.

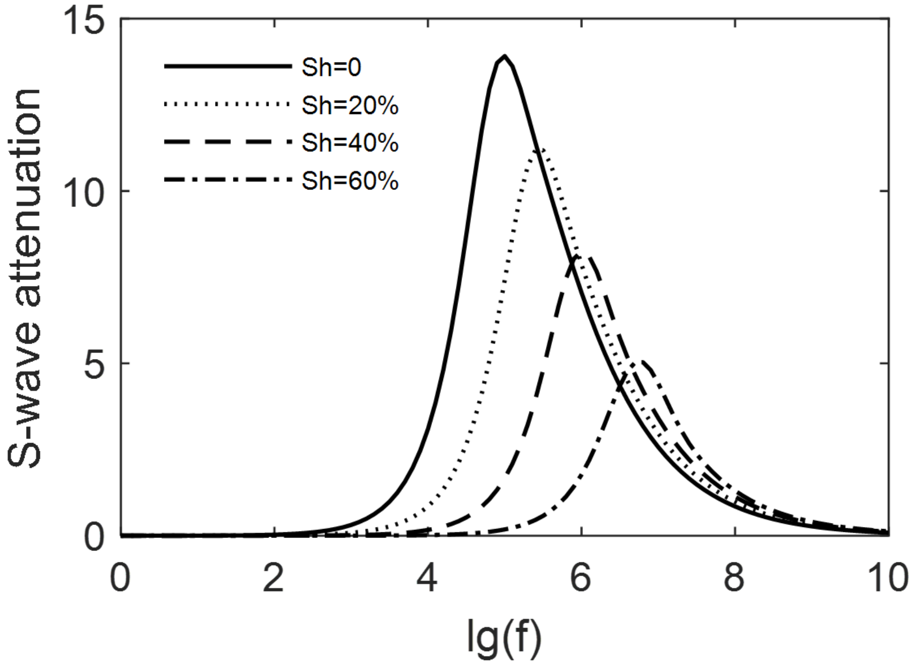

Fig. 3. The trend of P-wave velocity changing with frequency in mode A. The solid line is for 0 hydrate saturation, the dotted line is 20%, the dashed line is 40%, and the dash-dot line is 60%.

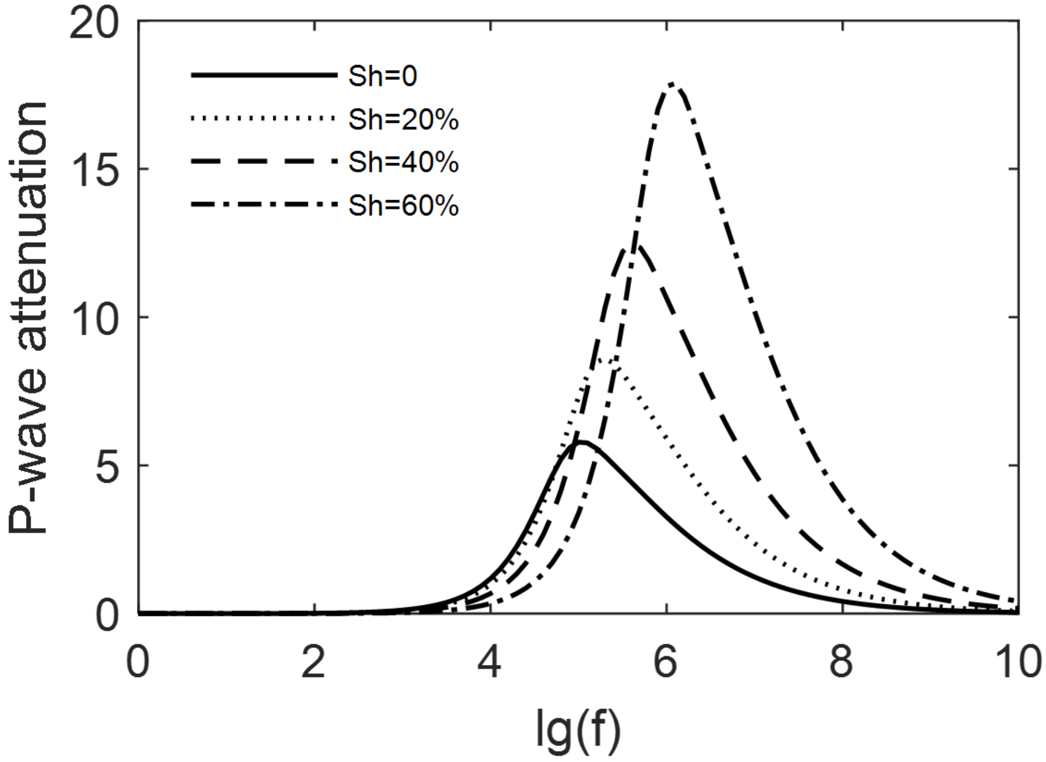

Fig. 4. The trend of the P-wave attenuation coefficient changes with frequency in mode A. The solid line is for 0 hydrate saturation, the dotted line is 20%, the dashed line is 40%, and the dash-dot line is 60%.

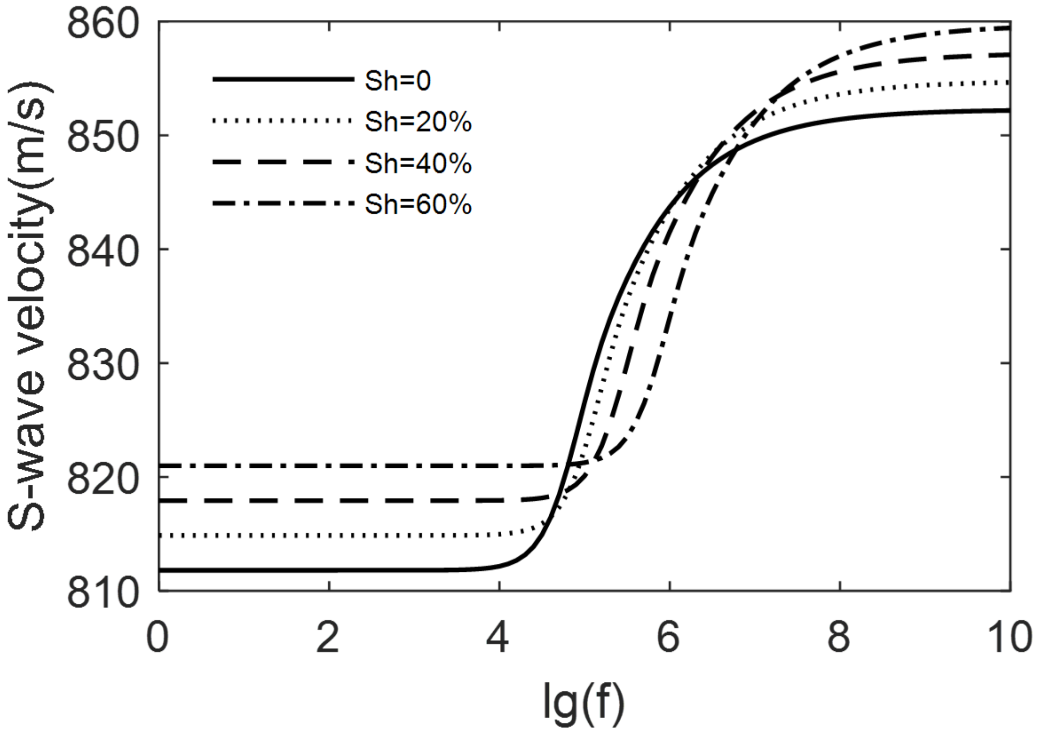

Fig. 5. The trend of S-wave velocity changing with frequency in mode A. The solid line is for 0 hydrate saturation, the dotted line is 20%, the dashed line is 40%, and the dash-dot line is 60%.

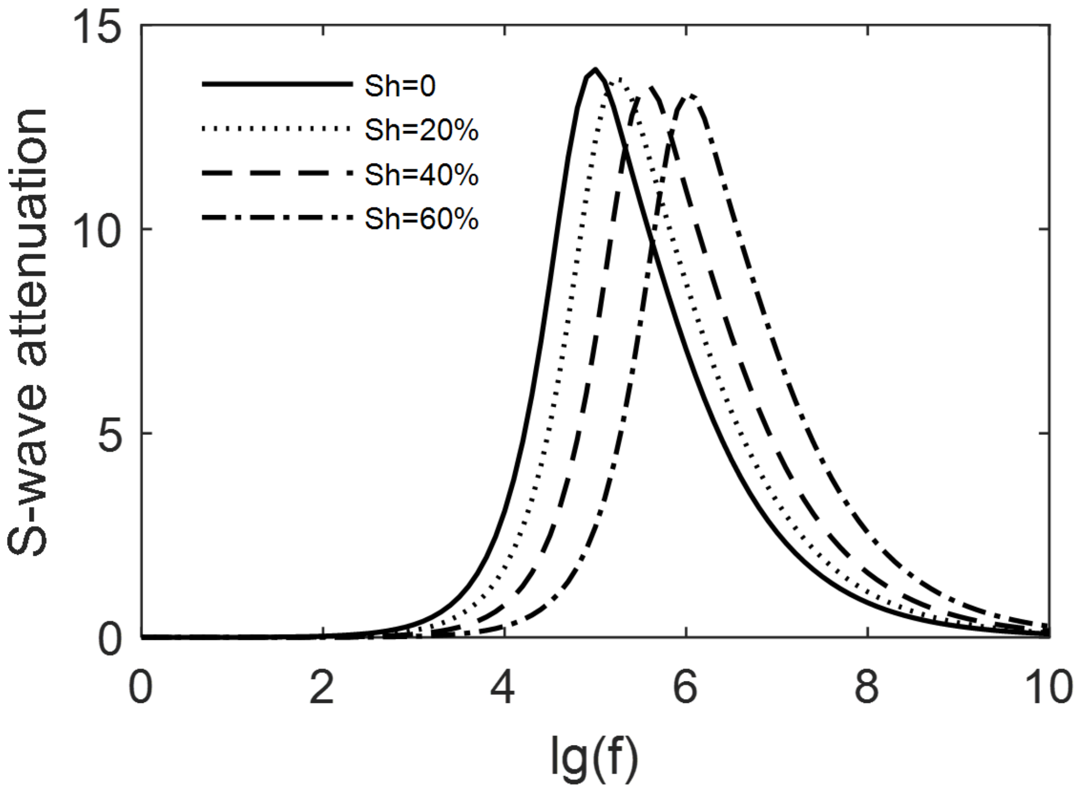

Fig. 6. The trend of the S-wave attenuation coefficient changes with frequency in mode A. The solid line is for 0 hydrate saturation, the dotted line is 20%, the dashed line is 40%, and the dash-dot line is 60%.

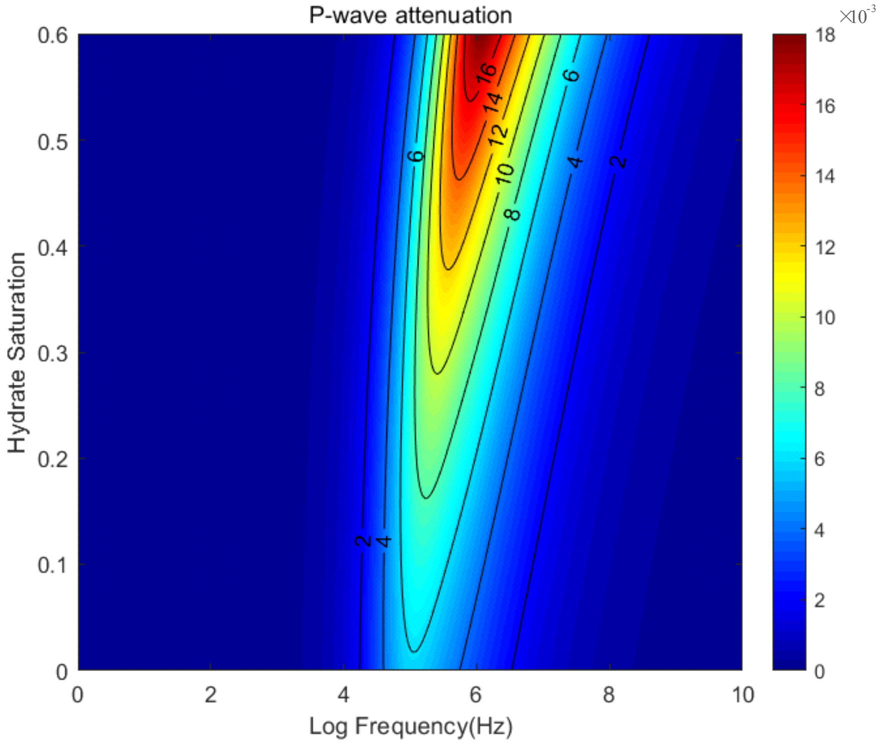

Fig. 7. The trend of P-wave attenuation coefficient with frequency and hydrate saturation in mode A.

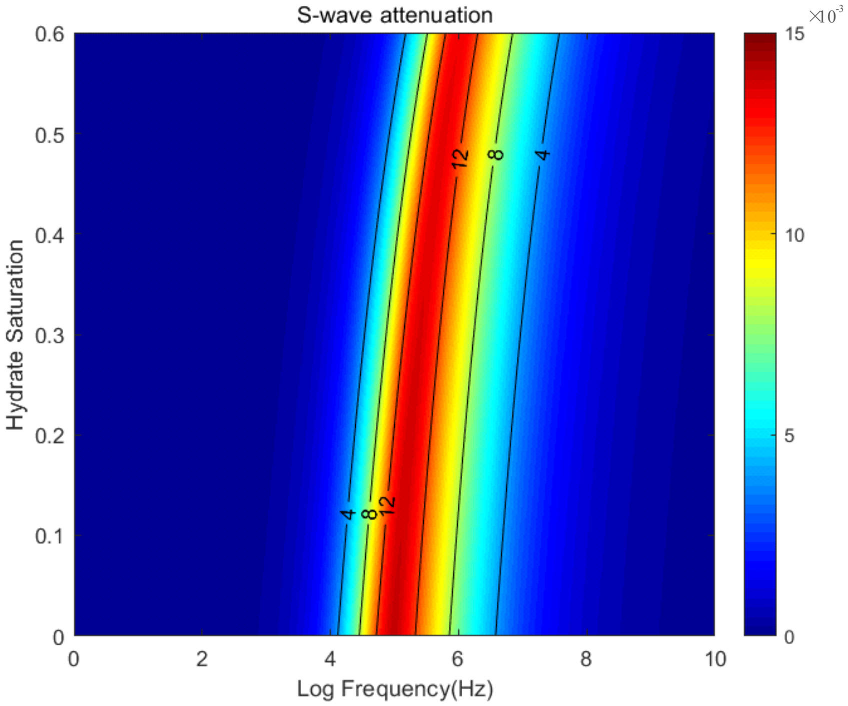

Fig. 8. The trend of S-wave attenuation coefficient with frequency and hydrate saturation in mode A.

Mode B

Fig. 9 shows the variation characteristics of P-wave velocity with frequency. For different hydrate saturation, the P-wave velocity increases non-linearly with the increase of frequency, and the P-wave velocity increases overall with the increasing hydrate saturation. The P-wave velocities in the low-frequency range and high-frequency range are almost unchanged. The P-wave velocity near the characteristic frequency increases rapidly to a specific value, and the increasing amplitude is negatively correlated with hydrate saturation. It is almost impossible to check this observation in Fig. 9. Probably due to the vertical scale of the plot. Fig. 10 and Fig. 13 show the variation characteristics of the P-wave attenuation coefficient with frequency. The attenuation increases first and then decreases with the increasing hydrate saturation, reaching the peak near the characteristic frequency. The peak value of the curve of attenuation and frequency gradually decreases and moves to the right with the increase of saturation. Fig. 11 shows the variation characteristics of S-wave velocity with frequency. For different hydrate saturation, the shear wave velocity increases non-linearly with the increasing frequency, and the S-wave velocity increases overall with the increasing saturation. S-wave velocities in the low-frequency range and high-frequency range are almost unchanged. The P-wave velocity near the characteristic frequency increases rapidly to a specific value, and the increasing amplitude is negatively correlated with hydrate saturation. Fig. 12 and Fig. 14 show the variation characteristics of the S-wave attenuation coefficient with frequency. The attenuation increase first and then decreases with the increase of hydrate saturation and reaches the peak near the characteristic frequency. With the saturation increase, the peak value of the attenuation and frequency curve gradually decreases and moves to the right.

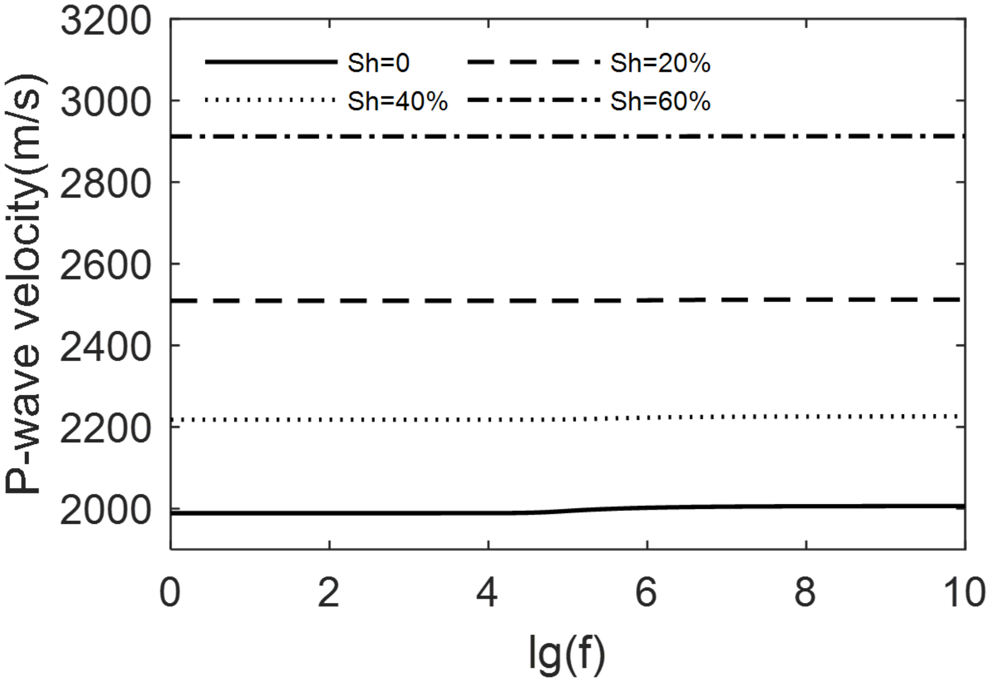

Fig. 9. The trend of P-wave velocity changing with frequency in mode B. The solid line is for 0 hydrate saturation, the dotted line is 20%, the dashed line is 40%, and the dash-dot line is 60%.

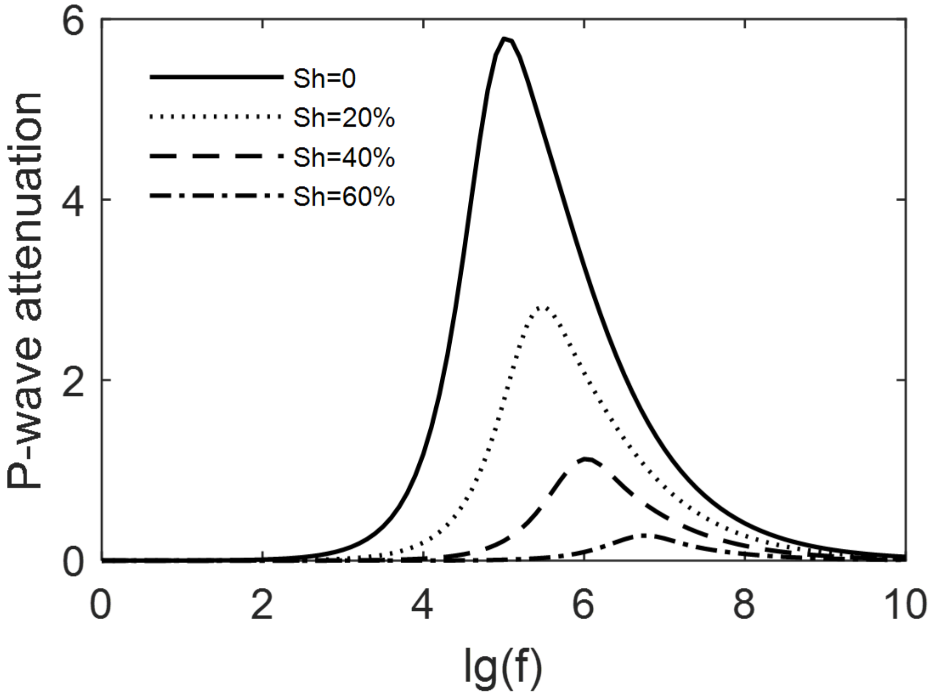

Fig. 10. The trend of the P-wave attenuation coefficient changes with frequency in mode B. The solid line is for 0 hydrate saturation, the dotted line is 20%, the dashed line is 40%, and the dash-dot line is 60%.

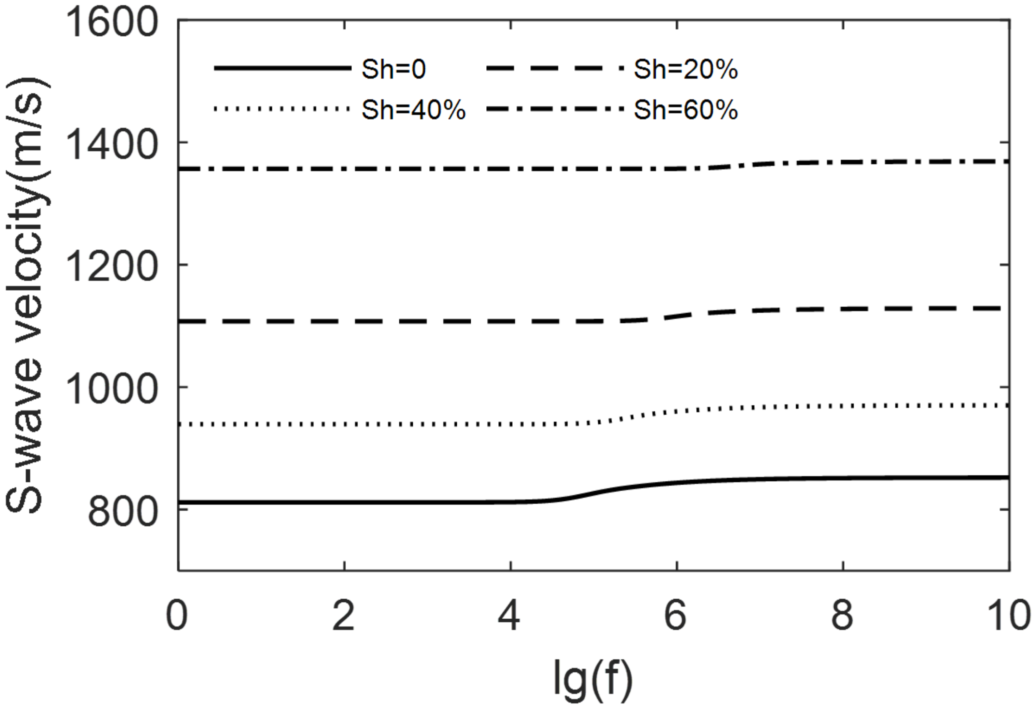

Fig. 11. The trend of S-wave velocity changing with frequency in mode B. The solid line is for 0 hydrate saturation, the dotted line is 20%, the dashed line is 40%, and the dash-dot line is 60%.

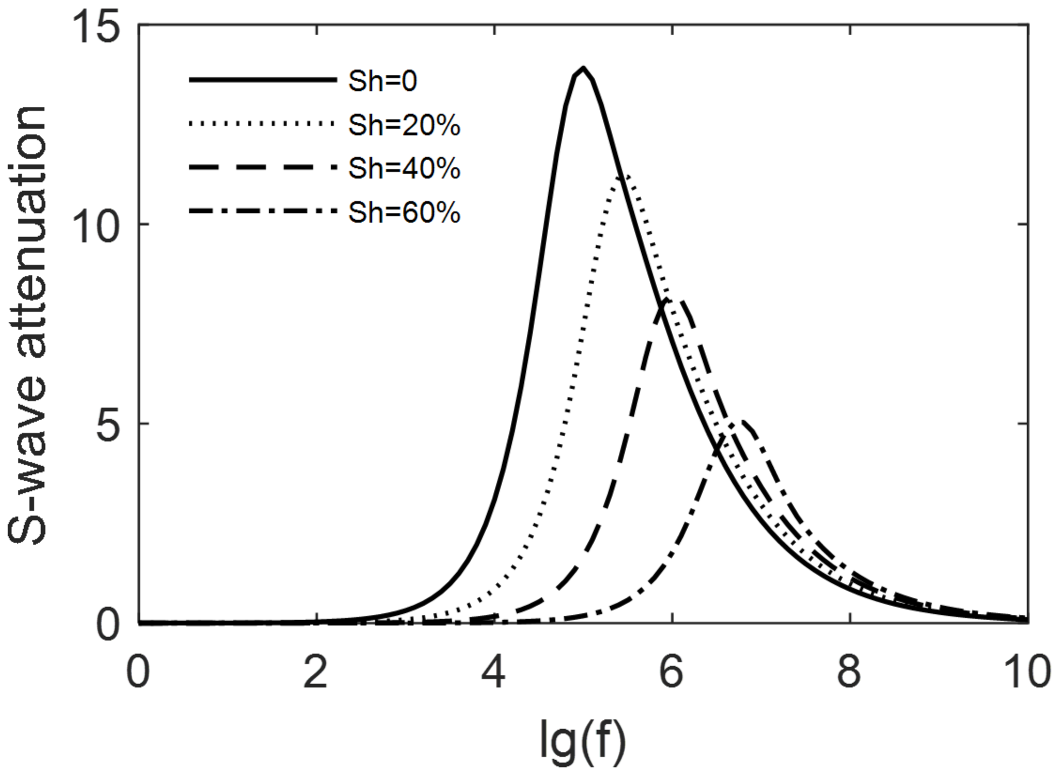

Fig. 12. The trend of the S-wave attenuation coefficient changes with frequency in mode B. The solid line is for 0 hydrate saturation, the dotted line is 20%, the dashed line is 40%, and the dash-dot line is 60%.

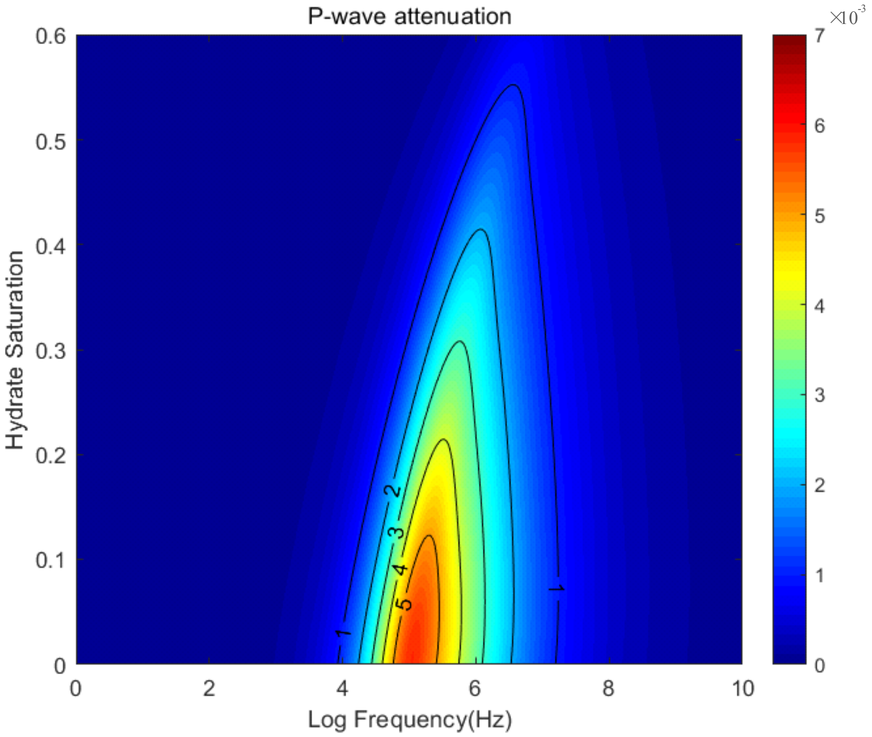

Fig. 13. The trend of P-wave attenuation coefficient with frequency and hydrate saturation in mode B.

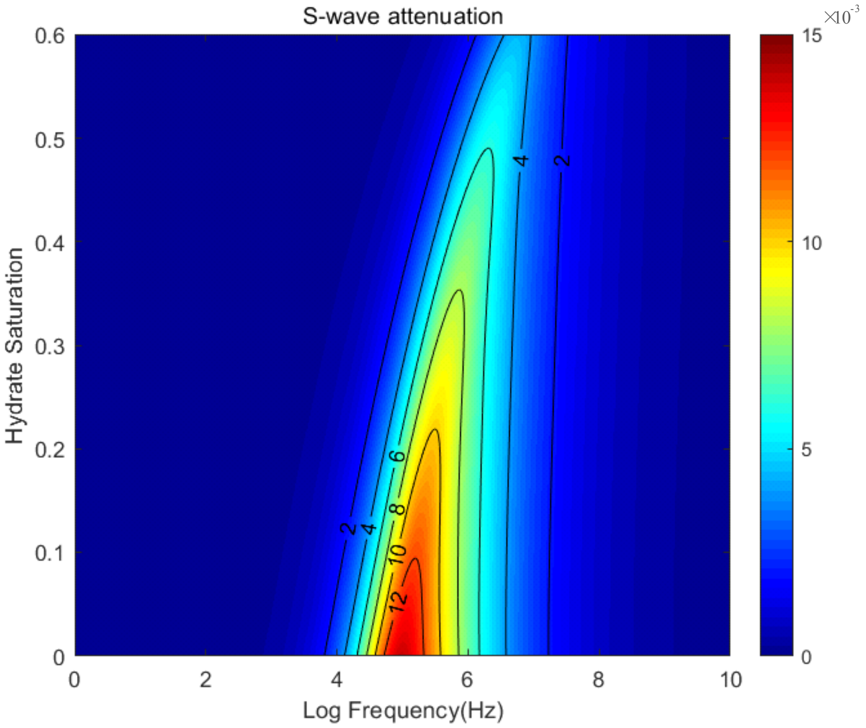

Fig. 14. The trend of S-wave attenuation coefficient with frequency and hydrate saturation in mode B.

Mode C

Fig. 15 shows the variation characteristics of P-wave velocity with frequency. For different hydrate saturation, the P-wave velocity increases non-linearly with the increase of frequency, and the P-wave velocity increases overall with the increasing hydrate saturation. The P-wave velocities in the low-frequency range and high-frequency range are almost unchanged. The P-wave velocity increases rapidly to a specific value near the characteristic frequency. When the hydrate saturation is less than 0.28, the increased amplitude is positively correlated with the hydrate saturation; when the hydrate saturation is larger than 0.28, the increased amplitude is negatively correlated with the hydrate saturation. Fig. 16 and Fig. 19 show the variation characteristics of the P-wave attenuation coefficient with frequency. The attenuation increases first and then decreases with the increasing hydrate saturation and reaches the peak at the characteristic frequency. When the saturation is less than 0.28, the peak value of attenuation and frequency curve gradually increases and moves to the right with the increasing saturation. When the saturation is larger than 0.28, the peak value of attenuation and frequency curve decreases gradually and moves to the right with the increasing saturation. Fig. 17 shows the variation characteristics of S-wave velocity with frequency. For different hydrate saturation, the S-wave velocity increases non-linearly with the increase of frequency, and the S-wave velocity increases overall with the increase of saturation. S-wave velocities in the low-frequency range and high-frequency range are almost unchanged. The P-wave velocity near the characteristic frequency increases rapidly to a specific value, and the increasing amplitude is negatively correlated with hydrate saturation.

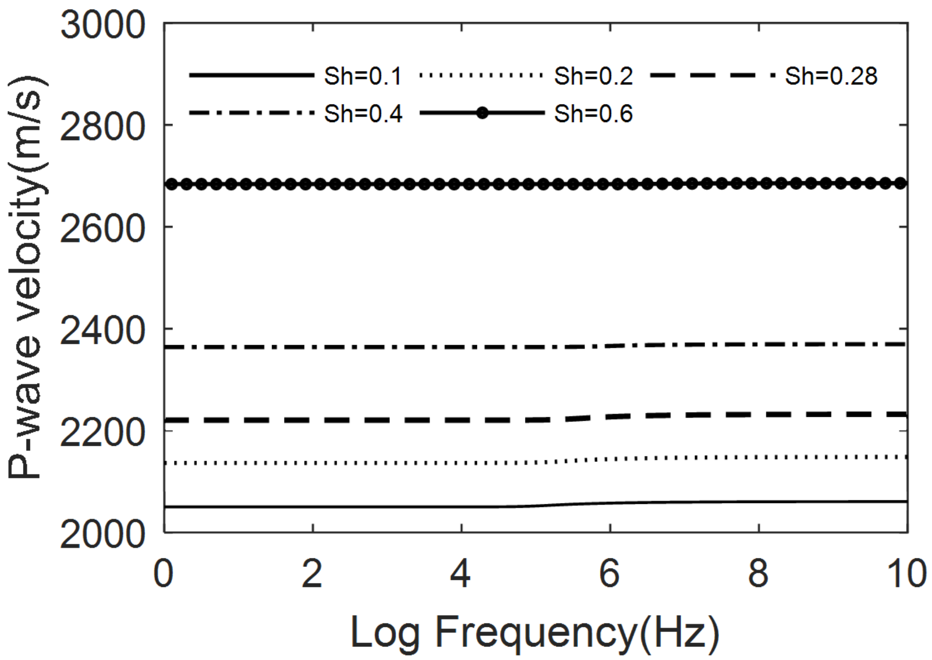

Fig. 15. The trend of P-wave velocity changing with frequency in mode C. The solid line is for 10% hydrate saturation, the dotted line is for 20%, the dashed line is for 28%, the dash-dot line is for 40%, and the line with circles is for 60%.

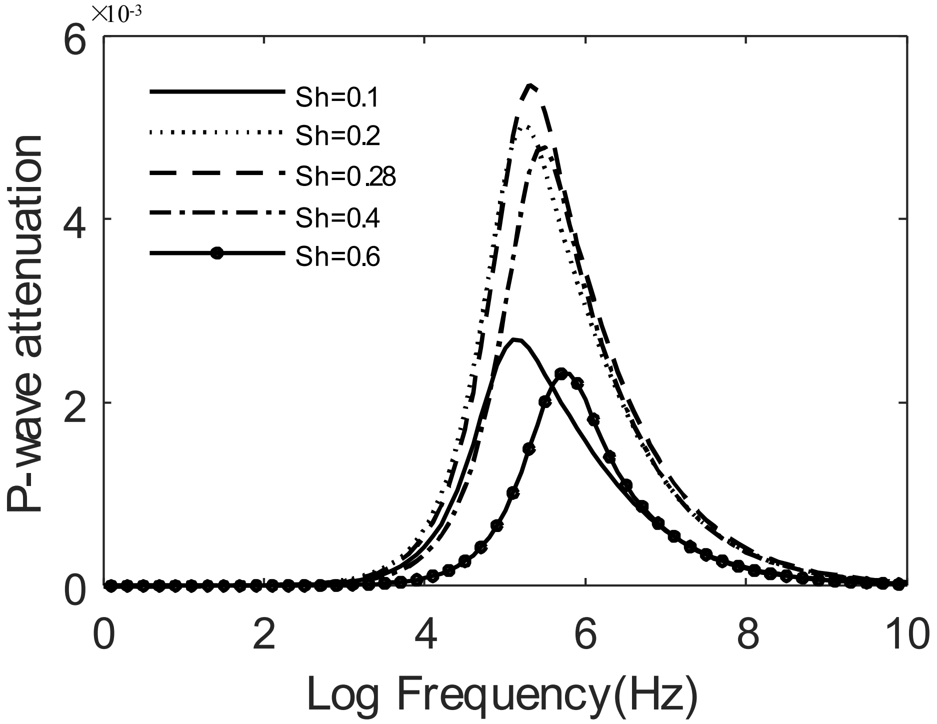

Fig. 16. The trend of the P-wave attenuation coefficient changes with frequency in mode C. The solid line is for 10% hydrate saturation, the dotted line is for 20%, the dashed line is for 28%, the dash-dot line is for 40%, and the line with circles is for 60%.

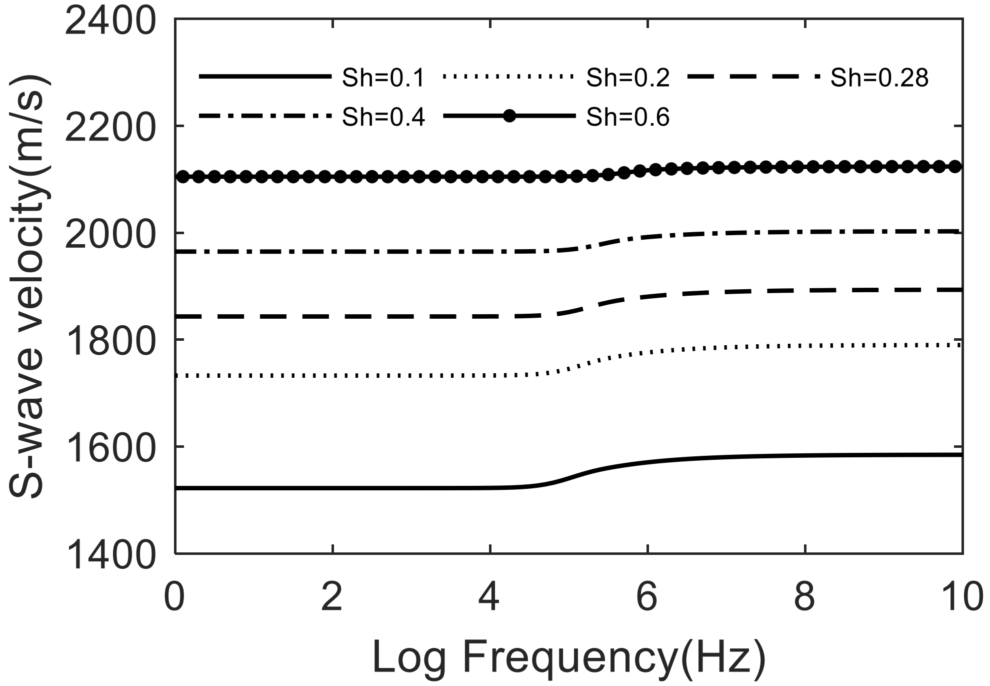

Fig. 17. The trend of S-wave velocity changing with frequency in mode C. The solid line is for 10% hydrate saturation, the dotted line is for 20%, the dashed line is for 28%, the dash-dot line is for 40%, and the line with circles is for 60%.

Fig. 18 and Fig. 20 show the variation characteristics of the S-wave attenuation coefficient with frequency. The attenuation increase first and then decreases with the increasing hydrate saturation and reaches the peak at the left and right sides of the characteristic frequency. With the saturation increase, the peak value of the attenuation and frequency curve gradually decreases and moves to the right.

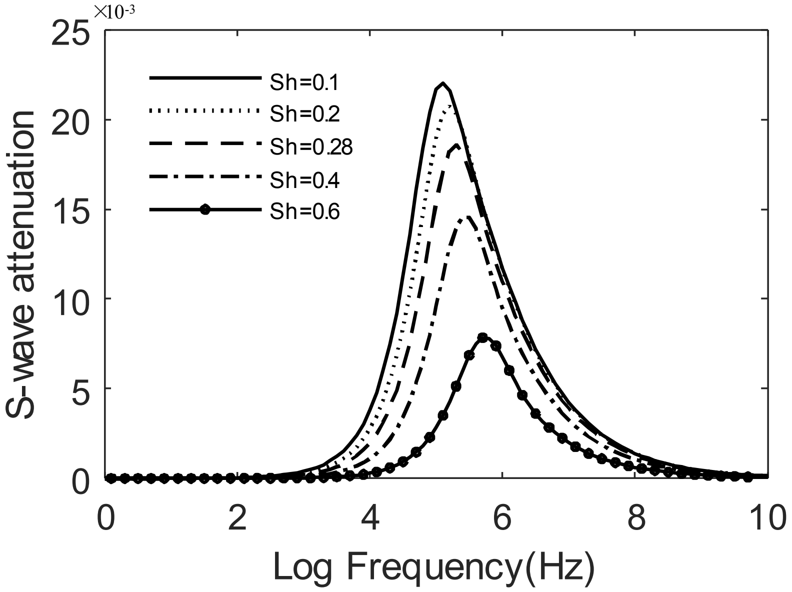

Fig. 18. The trend of the S-wave attenuation coefficient changes with frequency in mode C. The solid line is for 10% hydrate saturation, the dotted line is for 20%, the dashed line is for 28%, the dash-dot line is for 40%, and the line with circles is for 60%.

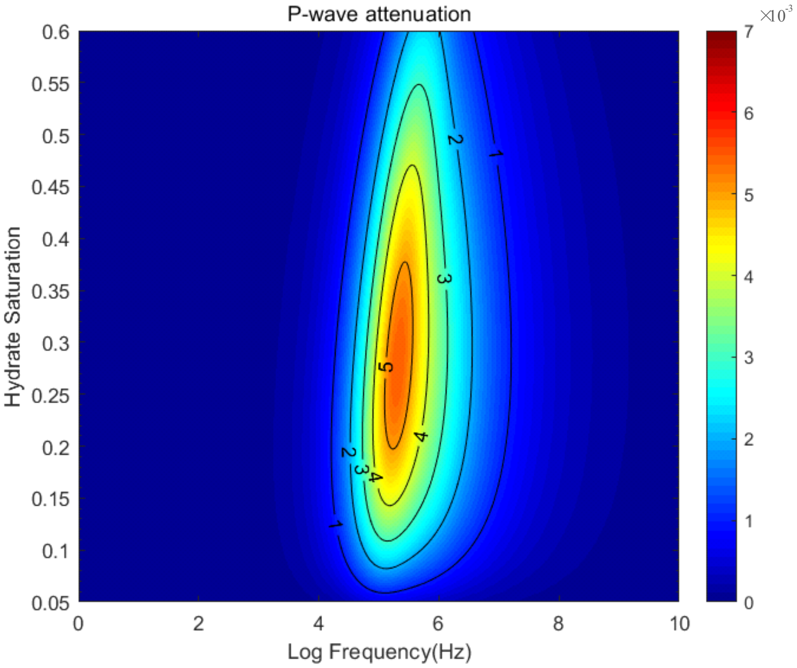

Fig. 19. The trend of P-wave attenuation coefficient with frequency and hydrate saturation in mode C.

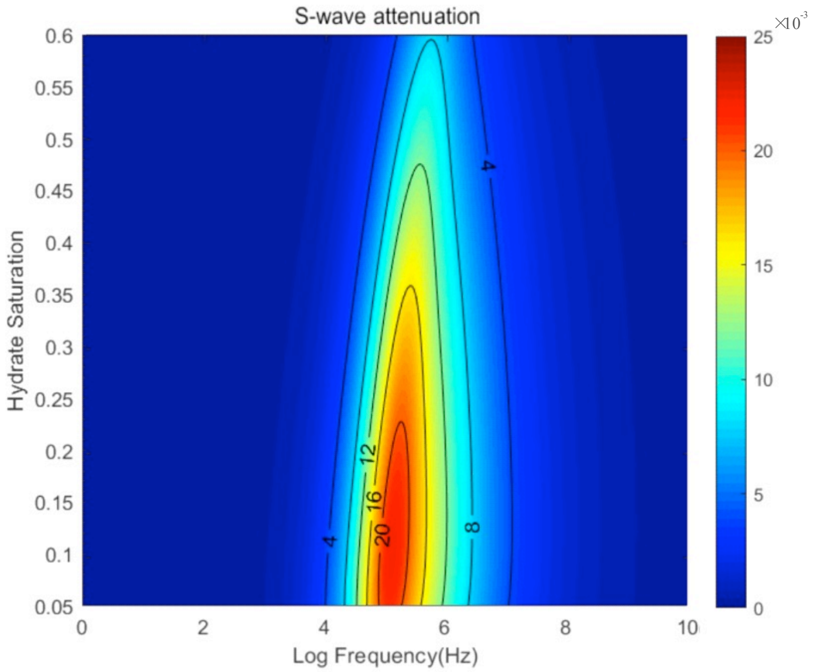

Fig. 20. The trend of S-wave attenuation coefficient with frequency and hydrate saturation in mode C.

Based on Biot's theory, this paper studies the relationship between hydrate saturation and dispersion and attenuation in suspension, particle-supported, and cementation modes. Hydrate formation's dispersion and attenuation characteristics with different occurrence modes are explored and clarified.

CONCLUSIONS

This paper studies the dispersion and attenuation of hydrate formation based on Biot's theory. The velocity dispersion and attenuation characteristics of hydrate-bearing deposits in the entire frequency band under different gas hydrate occurrence modes are simulated. The characteristics of dispersion and attenuation with saturation in hydrate formations is well understood. The P-wave velocity and S-wave velocity change non-linearly with frequency, and the P-wave velocity is unchanged in the low-frequency and high-frequency ranges. When the characteristic frequency is reached, the velocity rapidly rises to a specific value. At the same time, with the increasing hydrate saturation, the curves of P-wave velocity and S-wave velocity with frequency will move up as a whole. The peak values of P-wave and S-wave attenuation curve with frequency shift to higher frequencies with the increasing saturation for different hydrate occurrence modes. Each mode has its characteristics about the frequency and attenuation of hydrate saturation. For P-wave, the peak value of attenuation and frequency curve increases with the increasing saturation in suspension and particle-supported modes. In the cementation mode, when the hydrate saturation is lower than 0.28, the peak value increases with the increasing saturation, and when the hydrate saturation is larger than 0.28, the peak value decreases with the increasing saturation. For S-wave, the peak value decreases with the increase of hydrate saturation. The occurrence mode and hydrate saturation are the main factors affecting dispersion and attenuation.

Table 1. The parameters in this paper.

Parameter	Mark	Value	Unit
Skeleton particle density	ρ_0	2560	Kg/m3
The bulk modulus of the skeleton particles	K_0	3.688e10	Pa
Shear modulus of skeleton particles	G_0	3.246e10	Pa
Formation water density	ρ_w	1000	Kg/m3
Formation water volume modulus	K_w	2.25e9	Pa
Shear modulus of formation water	G_w	0	Pa
Formation water viscosity	η_w	1	cp
Gravitational acceleration	g	9.8	m/s^2
Grain diameter	d	20	micron
The average number of particle contacts per unit	N	9	
Critical porosity	ϕ_0	0.36	

ACKNOWLEDGMENTS

This work was supported by the following projects:

A. Guangdong Province Marine Economic Development (Six Major Marine Industries) Special Fund Project (No. [2021] No. 58).

B. Guangzhou Science and Technology Planning Project (202201011434).

C. Natural Science Foundation of China (NSFC). The project name is: Study of the seismic quantitative prediction and fluid identification for fractured reservoirs (41974124).

REFERENCES

Balakin, B.V., Hoffmann, A.C., Kosinski, P. and Høiland, S., 2010. Turbulent flow of hydrates in a pipeline of complex configuration. Chem. Engineer. Sci., 65: 5007-5017. doi:10.1016/j.ces.2010.06.005.

Berryman, J.G., 1980. Confirmation of Biot's theory. Appl. Phys. Lett., 37(A): 382-384. doi:10.1063/1.91951.

Berryman, J.G. 1981. Elastic wave propagation in fluid-saturated porous media. Acoust. Soc. Am., 69: 416-424. doi:10.1121/1.385457.

Biot, M.A., 1956. Theory of propagation of elastic waves in a fluid saturated porous solid. I. Low frequency range and II. Higher frequency range. Acoust. Soc. Am., 28: 168-191. doi:10.1121/1.1908239.

Dewangan, P., Mandal, R., Jaiswal, P., Ramprasad, T. and Sriram, G., 2014. Estimation of seismic attenuation of gas hydrate bearing sediments from multi-channel seismic data: A case study from Krishna-Godavari offshore basin. Marine Petrol. Geol., 58: 356-367. doi:10.1016/J.MARPETGEO.2014.05.015.

Dvorkin, J. and Nur, A., 1996. Elasticity of high-porosity sandstones: Theory for two North Sea data sets. Geophysics, 61: 1363-1370. doi:10.1190/1.1444059.

Dvorkin, J. and Uden, R., 2004. Seismic wave attenuation in a methane hydrate reservoir. The Leading Edge, 23: 730-732. doi:10.1190/1.1786892.

Ecker, C., 2001. Seismic characterization of methane hydrate structures. US Stanford University.

Gassmann, F., 1951. Über die Elastizität poröser Medien. Vier. der Natur. Gesellschaft in Zürich, 96: 1-23.

Gerner, A., Saenger, E.H. and Shapiro, S.A., 2007. Attenuation of P-waves due to interlayer fluid flow in hydrate-bearing sediments. J. Geophys. Engineer., 4: 394-403. doi:10.1088/1742-2132/4/4/005.

Guerin, G. and Goldberg, D., 2002. Sonic waveform attenuation in gas hydrate-bearing sediments from the Mallik 2L-38 research well, Mackenzie Delta, Canada. J. Geophys. Res., 107 (B5): 1-12. doi:10.1029/2001JB000556.

Guo, Z., Wang, X., Jiao, J. and Chen, H., 2021. Rock physics model and seismic dispersion and attenuation in gas hydrate-bearing sediments. Front. Earth Sci., 64(9): 1-14. doi:10.3389/feart.2021.641606.

Helgerud, M.B., Dvorkin, J., Nur, A. and Collett, T., 1999. Elastic-wave velocity in marine sediments with gas hydrates: Effective medium modeling. Geophys. Res. Lett., 26: 2021-2024. doi:10.1029/1999gl900421 .

Hill, R., 1952. The elastic behaviour of a crystalline aggregate. Proc. Phys. Soc., Sect. A, 65: 349-354. doi:10.1088/0370-1298/65/5/307.

Hovem, J.M., 1979. Viscous attenuation of sound in saturated sand. Acoust. Soc. Am., 66: 1807-1812. doi:10.1121/1.383653.

Jaiswal, P., Dewangan, P., Ramprasad, T. and Zelt, C.A., 2012. Seismic characterization of hydrates in faulted, fine-grained sediments of Krishna-Godavari Basin: full waveform inversion. J. Geophys. Res: Solid Earth, 117 (B10). doi:10.1029/2012JB009201.

Johnson, D.L. and Plona., T.J., 1982. Acoustic slow waves and the consolidation transition. Acoust. Soc. Am., 72: 556-565. doi:10.1121/1.388036.

Lee, M.W., 2002. Biot–Gassmann theory for velocities of gas hydrate-bearing sediments. Geophysics, 67: 1711-1719. doi:10.1190/1.1527072.

Lee, M.W., Hutchinson, D.R. and Dillon, W.P., 1996. Seismic velocities for hydrate-bearing sediments using weighted equation. J. Geophys. Res., Earth Surface, 101 (B9): 20347-20358. doi:10.1029/96JB01886.

Lee, M.W. and Waite, W.F., 2007. Amplitude loss of sonic waveform due to source coupling to the medium. Geophys. Res. Lett., 34(5): L05303. doi:10.1029/2006gl029015.

Li, C., 2015. Seismic wave attenuation in hydrate-bearing sediments and the estimates of attenuation coefficient . China University of Geosciences (Beijing).

Marín-Moreno, H., Sahoo, S.K. and Best, A.I., 2017. Theoretical modeling insights into elastic wave attenuation mechanisms in marine sediments with pore-filling methane hydrate. J. Geophys. Res., Solid Earth, 122: 1835-1847. doi:10.1002/2016JB013577.

Matsushima, J., 2006. Seismic wave attenuation in methane hydrate□bearing sediments: Vertical seismic profiling data from the Nankai Trough exploratory well, offshore Tokai, central Japan. J. Geophys. Res., 111 (B10). doi:10.1029/2005jb004031.

Mindlin, R.D., 1949. Compliance of elastic bodies in contact. J. Appl. Mech., 16: 259-268. doi:10.1115/1.4009973.

Nur, A., Mavko, G., Dvorkin, J. and Galmudi, D., 1998. A key to relating physical properties to porosity in rocks. The Leading Edge ,17: 357-362. doi:10.1190/1.1437977.

Pecher, I.A., Holbrook, W.S., Sen, M.K., Lizarralde, D., Wood, W.T., Hutchinson, D.R., Dillon, W.P., Hoskins, H. and Stephen, R.A., 2003. Seismic anisotropy in gas-hydrate-and gas-bearing sediments on the Blake Ridge, from a walkaway vertical seismic profile. Geophys. Res. Lett., 30: 1733. doi:10.1029/2003GL017477.

Pratt, R.G., Hou, F., Bauer, K. and Weber, M., 2005. Waveform tomography images of velocity and inelastic attenuation from the Mallik 2002 Crosshole Seismic Surveys. Geological Survey of Canada.

Priest, J.A., Best, A.I. and Clayton, C.R.I., 2006. Attenuation of seismic waves in methane gas hydrate-bearing sand. Geophys. J. Internat., 164:149-159. doi:10.1111/j.1365-246x.2005.02831.x.

Rossi, G., Gei, D., Böhm, G., Madrussani, G. and Carcione, J.M., 2007. Attenuation tomography: An application to gas-hydrate and free-gas detection. Geophys. Prosp., 55: 655-669. doi:10.1111/J.1365-2478.2007.00646.X.

Sahoo, S.K., Marín-Moreno, H. and North, L.J., Falcon-Suarez, I., Madhusudhan, B.N., Best, A.I. and Minshull, T.A., 2018. Presence and consequences of coexisting methane gas with hydrate under two phase water-hydrate stability conditions. J. Geophys. Res.: Solid Earth, 123: 3377-3390. doi:10.1029/2018JB015598.

Sahoo, S.K., North, L.J. and Marín-Moreno, H., 2019. Laboratory observations of frequency-dependent ultrasonic P-wave velocity and attenuation during methane hydrate formation in Berea sandstone. Geophys. J. Internat., 219:713-723. doi:10.1093/GJI/GGZ311.

Sain, K., Singh, A.K., Thakur, N.K. and Khanna, R., 2009. Seismic quality factor observations for gas-hydrate-bearing sediments on the western margin of India. Mar. Geophys. Res., 30: 137-145. doi:10.1007/s11001-009-9073-1.

Sakai, A. 1999. Velocity analysis of vertical seismic profile (VSP) survey at JAPEX/JNOC/GSC Mallik 2L-38 gas hydrate research well, and related problems for estimating gas hydrate concentration. GSC Bull., 544: 323-340. doi:10.4095/210775.

Stoll, R.D., 1977. Acoustic waves in ocean sediments. Geophysics 42 (4):715-725. doi:10.1190/1.1440741.

Sun, W.T., Ba, J., Muller, T.M., Carcione, J.M. and Cao, H., 2014. Comparison of P-wave attenuation models of wave-induced flow. Geophys. Prosp., 63: 378-390. doi:10.1111/1365-2478.12196.

Wang, H., Sun, Z. and Mark, C., 2012. Velocity dispersion and attenuation of seismic wave propagation in rocks. Acta Petrol. Sinica, 33: 332-342 doi:10.7623/syxb201202024.

Wood, W.T., Stoffa, P.L. and Shipley, T.H., 1994. Quantitative detection of methane hydrate through high-resolution seismic velocity analysis. J. Geophys. Res.: Earth Surface 99 (B5): 9681-9695. doi:10.1029/94JB00238.

Wood, W.T., Holbrook, S.W. and Hoskins, H., 2000. In-situ measurements of P-wave attenuation in the methane hydrate- and gas-bearing sediments of the Blake Ridge. Proc. Ocean Drilling Program, Scientific Results, 164: 265-272. doi:10.2973/odp.proc.sr.164.246.2000.

Wyllie, M.R.J., Gregory, A.R. and Gardner, L.W., 1956. Elastic wave velocities in heterogenous and porous media. Geophysics, 21: 41-70. doi:10.1190/1.1438217.

Zhan, L. and Jun, M., 2019. Rock-physics modeling of ultrasonic P- and S-wave attenuation in partially frozen brine and unconsolidated sand systems and comparison with laboratory measurements. Geophysics, 84(5): MR153-MR171. doi:10.1190/geo2018-0408.1.

Zhang, R., Li, H., Wen, P. and Zhang, B., 2016. The velocity dispersion and attenuation of marine hydrate-bearing sediments. Chin. J. Geophys., 59: 3417-3427. doi:10.1002/cjg2.30005.